Biochar X https://doi.org/10.48130/bchax-0026-0005

Original Research Open Access

Synergistic conversion of spent mobile phone batteries and industrial lignin into the $NiCo_2S_4/Co_9S_8$@LC composite with enhanced sodium storage performance

Changwei Dun[1#], Yizhao Zhao[2#], Pengpeng Zhang[1], Hua Lv[1], Yumin Liu[1], Yuebin Xi[2*], Xijun Zhang[1] and Rui Liang[1*]

Received: 21 November 2025
Revised: 31 December 2025
Accepted: 13 January 2026
Published online: 10 February 2026

Abstract

This study systematically investigated the $NiCo_2S_4/Co_9S_8$@LC composite synthesized from spent mobile phone batteries and industrial lignin, focusing on its sodium storage characteristics. A hydrothermal method was employed to successfully fabricate NCS/CS@$LC_{50,}$ exhibiting a honeycomb-like morphology through the precise control of lignin content. This composite integrated the high electrochemical activity of $NiCo_2S_4$ and Co_9S_8 with the superior conductivity of carbon materials, demonstrating promising sodium storage performance. The results indicated that NCS/CS@LC_{50} exhibited a high specific discharge capacity, i.e., an initial discharge specific capacity of 1,062.8 mAh g^{-1}, and outstanding cycling stability. The unique architecture of NCS/CS@LC_{50} facilitated the effective insertion and extraction of Na^+, allowing the material to preserve its structural stability throughout repeated charge-discharge processes, which in turn greatly improved the battery's cycling performance. At elevated current densities, such as 2.0 A g^{-1}, NCS/CS@LC_{50} continued to exhibit a high specific discharge capacity (208.7 mAh g^{-1}), demonstrating excellent rate performance. This research introduces an innovative approach to effectively recycle and reuse spent mobile phone batteries and industrial lignin, while also providing new insights into the design of electrode materials for sodium-ion batteries.

Keywords: Spent batteries, Industrial lignin, $NiCo_2S_4/Co_9S_8$@LC, Biochar, Sodium storage

Highlights

- This study offers a novel strategy for the recycling of industrial lignin and spent LIBs.
- This approach significantly reduces the synthesis cost of anode materials.
- The co-recycled product NCS/CS@LC_{50} demonstrates superior sodium storage performance.
- Co_9S_8 and lignin-derived carbon exert a pronounced enhancing effect on the sodium storage.

# Authors contributed equally: Changwei Dun and Yizhao Zhao
* Correspondence: Yuebin Xi (qlgdxyb@qlu.edu.cn); Rui Liang (031142@htu.edu.cn)
Full list of author information is available at the end of the article.

https://doi.org/10.48130/bchax-0026-0005

Graphical abstract

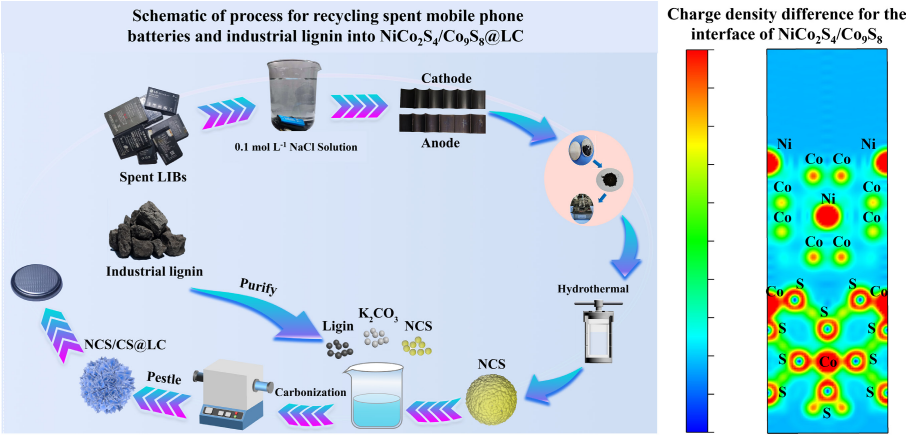

Introduction

With advancements in science and technology, alongside improvements in living standards, mobile phones have become essential components of daily life. However, mobile phone batteries typically have a limited lifespan and generally necessitate replacement within a few years[1]. Moreover, as mobile phone technology continues to evolve, the frequency with which consumers upgrade their devices is also increasing, leading to a substantial accumulation of spent mobile phone batteries. Improper disposal of these batteries poses significant risks to the environment and human health, and also results in a considerable waste of metal resources[2].

Lignin is a complex natural polymer primarily composed of phenylpropane structural units, representing approximately 30% of the Earth's non-fossil organic carbon. It constitutes a significant by-product in both the papermaking industry and biorefinery processes, with an annual production volume ranging from 50–70 million tons[3]. Despite its abundance, less than 5% of lignin is currently valorized for the production of high-value commercial products such as adhesives, dispersants, and surfactants[4]. Alarmingly, over 90% of industrial lignin is either discarded as waste or incinerated as low-value fuel, leading to substantial resource wastage and environmental pollution[5].

Therefore, it is crucial to recycle spent mobile phone batteries and industrial lignin to not only mitigate pollution risks to the environment but also to reduce the demand for new resources, thereby promoting resource recycling and supporting sustainable development. If the synergistic resource recovery of these two types of solid wastes can be realized, their respective advantages can be fully leveraged, thereby achieving optimal resource allocation and maximizing resource utilization efficiency.

Sodium-ion batteries (SIBs) possess the potential to supplant lithium-ion batteries (LIBs) because of considerable advantages regarding resource abundance, safety, low temperature performance, rapid charging capabilities, and environmental friendliness[6]. As is well known, the anode material serves as a pivotal component in SIBs, with its performance exerting a direct influence on the overall efficacy of these energy storage systems[7]. Transition metal sulfides that operate via the transformation reaction mechanism have garnered significant research interest owing to their high theoretical specific capacity, excellent ionic transport properties, and superior mechanical and thermal stability. Notably, bimetallic sulfides demonstrate enhanced electrochemical performance relative to their single-metal counterparts, which can be credited to the synergistic effects arising from the interaction of dissimilar metal ions. Among the reported bimetallic sulfides, $NiCo_2S_4$ has been deliberately engineered and synthesized to serve as a potential anode material for SIBs. Nevertheless, pure $NiCo_2S_4$ presents certain limitations concerning cycle stability, volumetric changes, first-cycle Coulombic efficiency, kinetic performance, and cost-effectiveness[8]. Consequently, it is imperative to modify $NiCo_2S_4$ to enhance its sodium storage capabilities. And researchers often adopt a composite material design strategy that synergistically integrates $NiCo_2S_4$ with various carbon materials to bolster both structural integrity and electrochemical performance. For instance, Xi et al. prepared hollow mesoporous carbon spheres encapsulating $NiCo_2S_4$ nanoparticles, demonstrating superior rate performance and achieving a high capacity of 271 mAh g^{-1} at 10 A g^{-1}[9]. However, the carbon sources are predominantly conventional industrial products, which do not fully align with the principle of 'treating waste with waste' in the context of deep resource recycling. To date, no studies have been reported on enhancing $NiCo_2S_4$'s sodium storage performance through the combination of industrial lignin-derived carbon and $NiCo_2S_4$.

In this study, $NiCo_2S_4$ was synthesized from spent mobile phone batteries via a hydrothermal method, an approach characterized by straightforward operation, high product purity, controllable reaction parameters, and environmental sustainability[10]. The synthesized $NiCo_2S_4$ was carbonized in conjunction with lignin, resulting in the successful preparation of $NiCo_2S_4/Co_9S_8$@LC. This process enables the synergistic high-value utilization of both types of waste. Moreover, a series of characterizations was conducted to investigate the effect of Co_9S_8 and lignin-derived carbon on the structure, morphology, and sodium storage properties of $NiCo_2S_4$. This approach not only substantially lowers the synthesis cost of anode materials but also promotes the sustainable utilization of resources and environmental protection. Importantly, it offers a novel strategy for the recycling and reutilization of industrial lignin and spent LIBs.

Experiments

Synthesis of materials

Synthesis of $NiCo_2S_4$

The processes of discharging, disassembling, and dissolving spent mobile phone batteries (Nokia), along with the hydrothermal synthesis of $NiCo_2S_4$, have been detailed in a previous study[11].

Purification of industrial lignin

Two hundred g of industrial lignin (Jilin Papermaking (Group) Co., Ltd) was weighed and dissolved in NaOH solution with a pH ≥ 12 under continuous stirring for 2 h. Once the lignin was fully dissolved, the solution was filtered to remove insoluble impurities, and the filtrate was collected. Subsequently, while continuously stirring, 50% (w/w) sulfuric acid was slowly added to the filtrate to adjust the pH of the solution to 2. The mixture was stirred for an additional 2 h to allow lignin precipitation. The solution was then allowed to stand for 24 h, after which the precipitated lignin was collected by filtration. The collected lignin was washed thoroughly and subjected to freeze-drying to obtain purified lignin.

Synthesis of $NiCo_2S_4$/Co_9S_8@LC

A total of 0.2 g of $NiCo_2S_4$ was introduced into an ethanol-water mixture ($V_{ethanol}$: V_{water} = 1:4). The dispersion was subjected to multiple cycles of ultrasonic treatment to ensure homogeneity. Subsequently, lignin was introduced into a separate ethanol-water solution ($V_{ethanol}$: V_{water} = 1:4, C = 2 mg/mL) under ultrasonic conditions for thorough dispersion. The weight ratios of lignin to $NiCo_2S_4$ were set at 25%, 50%, and 75%. The two dispersions were then combined, and the pH of the final solution was regulated to 12 by incorporating a 20% (w/w) NaOH solution. The mixture was subjected to magnetic stirring at ambient temperature for a duration of 30 min, and then subjected to ultrasonic processing for another 30 min. This procedure was carried out repeatedly until a uniformly dispersed solution was obtained. Thereafter, the pH was lowered to 2 by adding a 50% (w/w) sulfuric acid solution. The solution was left undisturbed for 12 h to enable the full precipitation of $NiCo_2S_4$ and lignin. Finally, the $NiCo_2S_4$-lignin composite was collected via centrifugation and dried.

The above-mentioned synthesized $NiCo_2S_4$-lignin composites were dispersed in 50 mL of deionized water, and then K_2CO_3 was added as an activator at a K_2CO_3-to-lignin weight ratio of 1:1. The resulting mixture was continuously stirred for 4 h, subsequently dried at 80 °C, and finally ground into a fine powder for collection. Next, the sample was heated under a nitrogen atmosphere from ambient temperature to 250 °C at a heating rate of 10 °C/min and held at this temperature for 30 min. Subsequently, the temperature was further increased to 600 °C at the identical heating rate of 10 °C/min and maintained for 2 h to achieve complete carbonization of the lignin component. Afterward, the resulting product was thoroughly rinsed multiple times with deionized water and then dried at 100 °C to yield the final $NiCo_2S_4$/Co_9S_8@LC composite, which was designated as NCS/CS@LC_{25}, NCS/CS@LC_{50}, and NCS/CS@LC_{75}, respectively.

Characterization of materials, electrochemical measurements, and computational details

The structural and morphological characterization techniques, the electrochemical performance evaluation procedures, and the theoretical calculation details for the synthesized samples were included in the Supplementary Material.

Results and discussion

The flowchart illustrating the co-conversion process of spent mobile phone batteries and industrial lignin for the preparation of NCS/CS@LC is presented in Fig. 1a. The XRD patterns of the synthesized samples are presented in Fig. 1b. The observed diffraction peaks exhibited sharpness and high intensity, indicating a relatively complete crystal structure and elevated crystallinity. It was evident that the diffraction peaks of NCS aligned well with the standard card for $NiCo_2S_4$ (JCPDS No. 20-0782), confirming the successful synthesis of $NiCo_2S_4$. Upon incorporating varying amounts of lignin into NCS and subsequently carbonizing the composites in a nitrogen atmosphere, a new phase of Co_9S_8 (JCPDS No.19-0364) emerged, indicated by '*' in Fig. 1b. Notably, it appeared that $NiCo_2S_4$ may partially convert into Co_9S_8 due to the reorganization or recombination of metal ions from $NiCo_2S_4$ with sulfur ions present in the reaction system under conditions of elevated temperature and pressure, resulting in novel metal sulfide phase formation[12]. In addition, the sulfur-containing functional groups in lignin, such as methylthio groups, release S^{2-} or H_2S during thermal decomposition, thereby sustaining a sulfidation atmosphere. Concurrently, the decomposition produces reductive gases such as CO and H_2, which lower the oxygen potential of the system and promote the generation of Co_9S_8. Ultimately, carbon materials derived from lignin may encapsulate these metal sulfides' surface to create a composite structure represented as NCS/CS@LC. The presence of other phases, such as $NiCo_2S_4$ and Co_9S_8, leads to notably weak and nearly undetectable diffraction peaks for carbon within the synthesized materials. This suggested that the carbon produced post-carbonization was amorphous in nature[13]. Nevertheless, the Raman spectrum corroborated the existence of carbon within NCS/CS@LC, as depicted in Fig. 1c.

Raman spectroscopy is a spectral analysis technique predicated on the Raman scattering effect, which elucidates molecular vibrational and rotational information of matter by examining the frequency difference between scattered and incident light. The G peak constitutes one of the most prominent characteristic peaks in carbon materials, primarily resulting from the stretching vibrations of sp^2-hybridized carbon atoms[14]. Conversely, the D peak signifies another critical characteristic peak in carbon materials, predominantly arising from defects or disordered structures within the carbon atomic lattice[15]. As illustrated in Fig. 1c, it was evident that the typical D and G characteristic peaks were absent in NCS not co-carbonized with lignin; however, other samples exhibited significant D and G peaks located near 1,340 and 1,585 cm^{-1}, respectively. These observations substantiated the presence of carbon within NCS/CS@LC. Furthermore, the intensity ratio of D and G peak (I_D/I_G) is frequently utilized as an essential parameter for characterizing defect density in carbon materials[16]. A progressive decrease in I_D/I_G from 0.983 to 0.843 was noted, suggesting a reduction in amorphous or defective carbon content alongside an enhancement in graphitization degree. However, an excessively high degree of graphitization may not be advantageous, as it leads to an increase in ordered graphite layers while reducing interlayer spacing, concurrently diminishing surface defects. This results in fewer Na^+ adsorption sites, which could consequently impair the sodium storage capacity[17]. High levels of graphitization may yield a densely compacted carbon material detrimental to Na^+ diffusion and storage capabilities, thereby adversely affecting cycling performance and Coulombic efficiency, as well as limiting Na^+ diffusion rates that negatively impact rate performance[18]. Therefore, achieving an optimal I_D/I_G value is crucial for attaining superior electrochemical performance, which will be further substantiated through subsequent analyses.

Figure 1e, g, respectively, present the adsorption–desorption isotherms of NCS and NCS/CS@LC_{50}, with the corresponding isotherms for the remaining samples provided in Supplementary Fig. S1, which were used to determine the specific surface area and pore size distribution. All four isotherms displayed typical type-IV characteristics, evident from the hysteresis loop observed in the high-pressure region, where the desorption curve lagged behind the adsorption curve during the desorption process. This

https://doi.org/10.48130/bchax-0026-0005

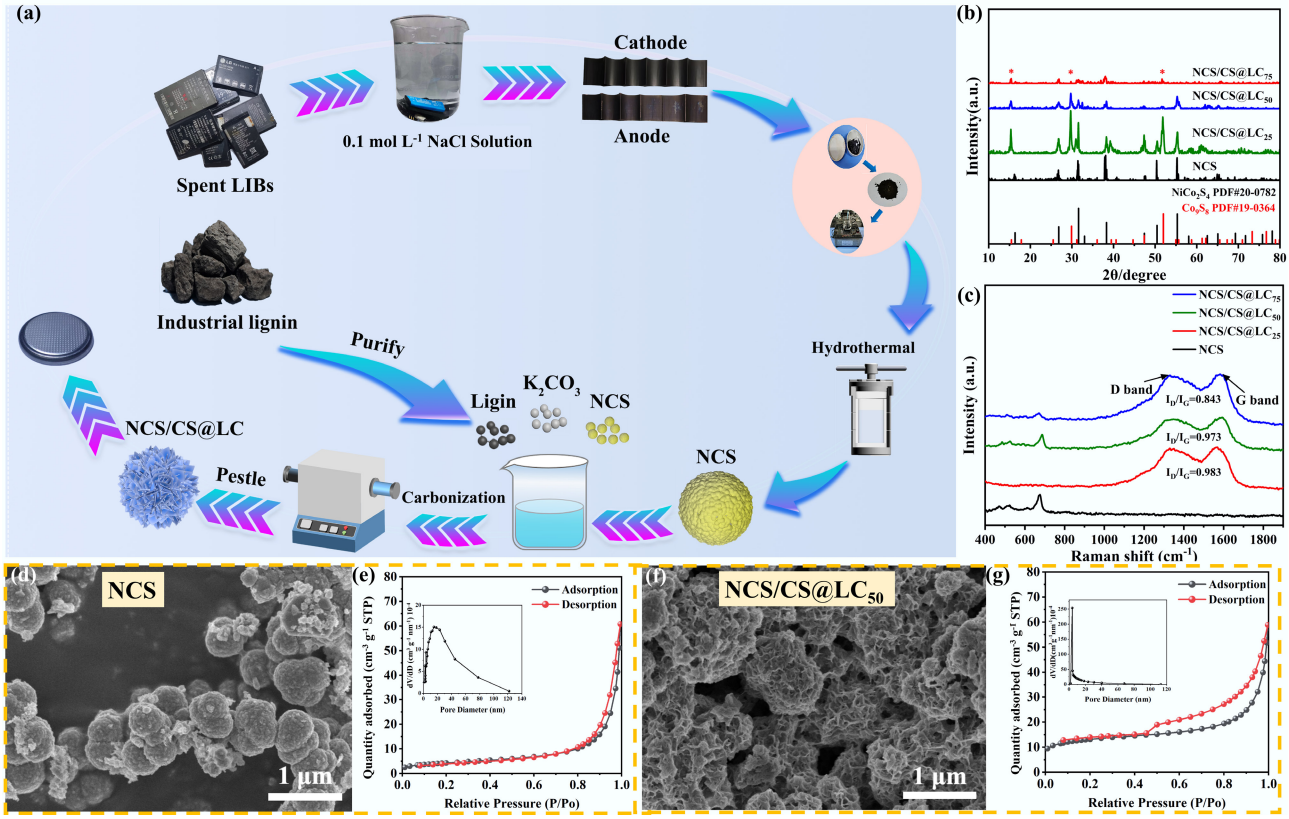

Fig. 1 (**a**) Schematic of the process for recycling spent mobile phone batteries and industrial lignin into $NiCo_2S_4/Co_9S_8$@LC. (**b**) XRD patterns of synthesized samples. (**c**) Raman spectral analysis of synthesized samples. (**d**) SEM images of NCS. (**e**) Adsorption-desorption isotherm of NCS. (**f**) SEM images of $NCS/CS@LC_{50}$. (**g**) Adsorption-desorption isotherm of $NCS/CS@LC_{50}$.

phenomenon further confirmed that NCS and all the NCS/CS@LC samples possessed a mesoporous structure. The BJH model was employed to calculate the pore size distribution based on the Kelvin equation, considering the effects of capillary condensation on adsorption capacity. The results are displayed in the corresponding insets of Fig. 1e, g, and Supplementary Fig. S1. Additionally, the BET specific surface area and BJH pore size data are compiled in Table 1. It was evident that as the lignin weight ratio increased, the specific surface area initially decreased and subsequently increased, whereas the pore size exhibited a gradual decreasing trend. This trend could be attributed to the fact that varying amounts of lignin induce distinct cross-linking and condensation reactions during the carbonization process, thereby leading to diverse morphologies and pore structures in the resulting products. It is well established that an appropriate specific surface area can offer a greater number of active sites, facilitating the insertion and expulsion of Na^+. An optimal pore structure facilitates electrolyte infiltration and ion mobility, leading to enhanced cycling durability and rate capability in SIBs. When both the specific surface area and pore dimensions are small, the availability of active sites for Na^+-involved electrochemical reactions decreases, hindering Na^+ migration and ultimately compromising the overall battery performance[19]. Conversely, if these parameters are excessively large, it may result in an increased occurrence of side reactions, which could significantly hinder the enhancement of electrochemical performance[20]. Subsequent studies demonstrated that $NCS/CS@LC_{50}$ exhibited superior cycling and rate performance due to its optimal balance between specific surface and pore size. The morphology of the synthesized material is illustrated in Fig. 1d, f, and Supplementary Fig. S2. Pure $NiCo_2S_4$, which had not been co-carbonized with lignin, retained a spherical morphology, as previously reported[11]. Upon mixing $NiCo_2S_4$ and lignin in an ethanol-water solution at varying weight ratios and subjecting the mixture to drying and calcination, significant morphological changes occurred, resulting in the formation of a new phase denoted as Co_9S_8. The composite phase $NiCo_2S_4/Co_9S_8$ that formed was subsequently coated with carbon derived from lignin. It is evident that the weight ratio of lignin to $NiCo_2S_4$ exerts a substantial impact on the morphology. When the lignin content is insufficient, phase separation or structural reorganization may occur at the interface between $NiCo_2S_4$ and lignin during carbonization, leading to the agglomeration and stacking of product particles[21], as depicted in Supplementary Fig. S2a. Upon increasing the dosage of lignin, the carbonized lignin forms a continuous carbon skeleton structure and efficiently encapsulates the spherical metal sulfides, thereby exhibiting a honeycomb-like morphology as depicted in Fig. 1f. When an excessive amount of lignin is introduced, during the carbonization process, a series of complex chemical reactions, including pyrolysis, polycondensation, and catalytic cracking, may intensify between $NiCo_2S_4$ and lignin. These reactions significantly increase the specific surface area and result in structural collapse[22], as illustrated in Supplementary Fig. S2b. Consequently, to achieve a honeycomb-like structure, it was optimal to utilize lignin at a weight ratio of 50%.

The surface elemental composition of the $NCS/CS@LC_{50}$ composite was comprehensively analyzed using XPS. As illustrated in Fig. 2a, the presence of elements such as Ni, Co, S, and C was confirmed. In Fig. 2b, the Co 2p spectrum exhibited spin-orbit splitting, typically manifested as two primary peaks at 780.11 and

Table 1 The specific surface area, pore size, Warburg impedance factor (σ) and Na^+ diffusion coefficient of the as-synthesized samples

Sample	Specific surface area ($cm^2\ g^{-1}$)	Pore size (nm)	Warburg impedance factor (σ)	Na^+ diffusion coefficient D ($cm^2\ s^{-1}$)	ICE (%)
NCS	15.11	23.68	300.30	3.9×10^{-12}	53.15
NCS/CS@LC_{25}	6.03	23.54	82.90	5.1×10^{-11}	54
NCS/CS@LC_{50}	42.25	12.98	36.21	2.7×10^{-10}	65.61
NCS/CS@LC_{75}	95.20	10.02	133.50	2.0×10^{-11}	46.77

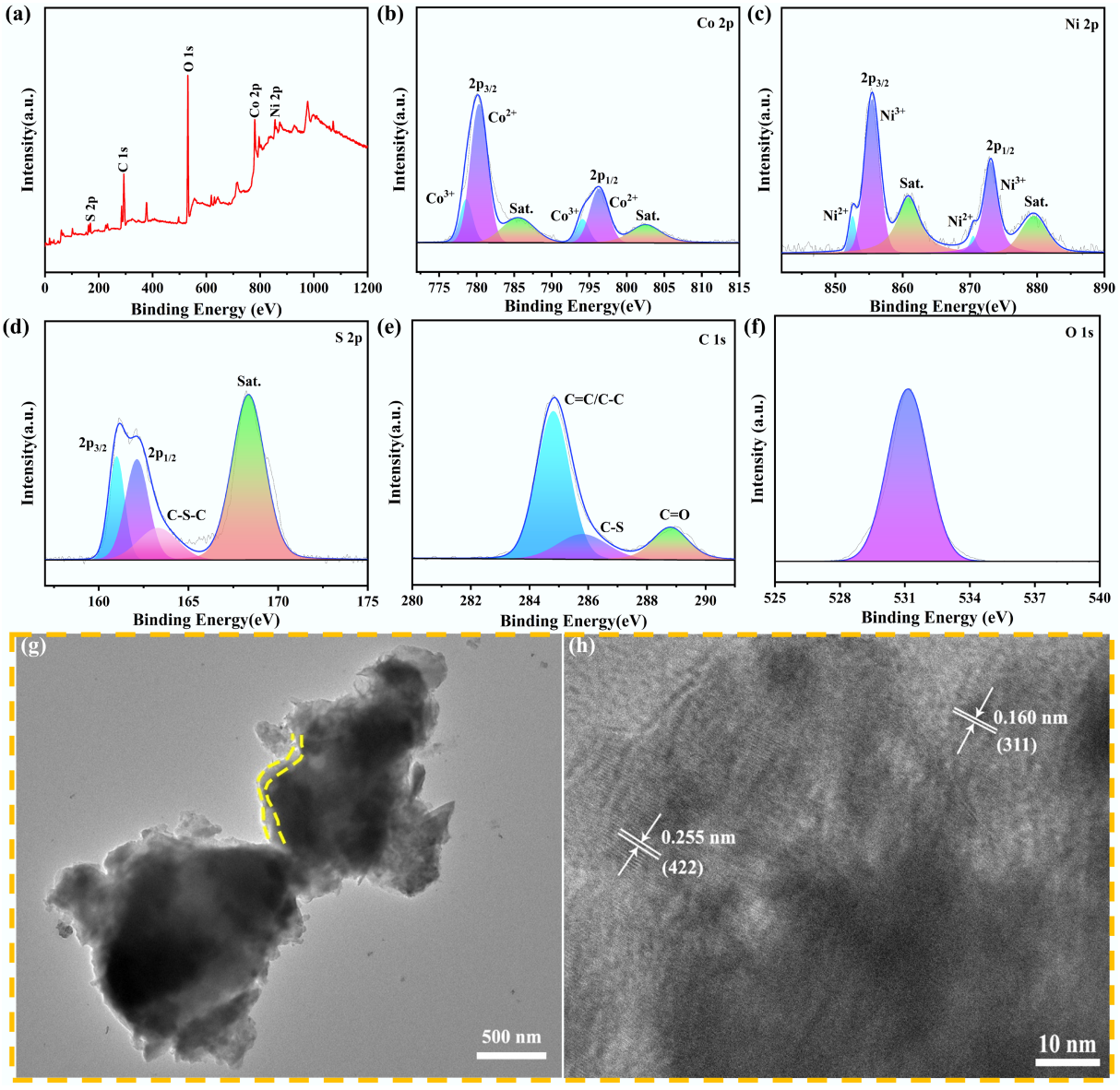

Fig. 2 (**a**) XPS full spectrum and high-resolution XPS spectra of: (**b**) Co 2p, (**c**) Ni 2p, (**d**) S 2p, (**e**) C 1s, and (**f**) O 1s. (**g**) TEM image of NCS/CS@LC_{50}. (**h**) Lattice fringes of NCS/CS@LC_{50}.

796.22 eV, corresponding to Co $2p_{3/2}$ and Co $2p_{1/2}$, respectively. In addition to the primary peaks, satellite peaks (designated as Sat.), located at 785.50 and 802.50 eV, were also observed. By employing peak fitting techniques, the experimental data were deconvoluted into multiple independent peaks; specifically, those observed at 780.30 and 796.30 eV were attributed to Co^{2+} ions, while those detected at 778.60 and 794.10 eV corresponded to Co^{3+} ions, indicating that both oxidation states were present in this sample[23]. The XPS spectra of the Ni 2p orbitals exhibited two prominent peaks corresponding to $2p_{3/2}$ and $2p_{1/2}$, along with their respective satellite peaks observed at 860.85 and 879.50 eV, as displayed in Fig. 2c. The binding energy of the $2p_{3/2}$ peak was lower than that of the $2p_{1/2}$ peak, and its intensity was comparatively higher. Similarly, upon fitting these splits within the Ni 2p orbital, two additional peaks were identified at energies of 852.55 and 870.49 eV, which were associated with Ni^{2+}. Conversely, two more distinct peaks were found at 855.45 and 873.10 eV, attributable to Ni^{3+}, thus confirming that Ni exists in the +2 and +3 oxidation states within this sample[24].

The S 2p peak exhibited a spin-orbit splitting, resulting in two distinct sub-peaks, S $2p_{3/2}$ and S $2p_{1/2}$, located at binding energies of 160.99 and 162.13 eV, respectively. The excitation effect, commonly observed in metal sulfides, resulted in the formation of satellite peaks situated at 168.35 eV, as illustrated in Fig. 2d. The peak situated at 163.29 eV, which was assigned to the C–S–C bond, corroborated the formation of carbon derived from lignin and its binding to metal sulfides. In the C 1s spectrum (Fig. 2e), the peaks at 284.81, 285.80, and 288.80 eV corresponded to the C=C/C–C, C–S, and C=O bonds, respectively. Finally, the peak at 531.14 eV, exhibited in the O 1s spectrum (Fig. 2f), may have resulted from the oxidation of the carbon layer surface or the incorporation of oxygen during the preparation of the composite. Figure 2g presents the TEM image of NCS/CS@LC_{50}, which is in good agreement with its SEM image, once again indicating its honeycomb-like morphology. Furthermore, the presence of carbon layers in NCS/CS@LC_{50} is illustrated in Fig. 2g, with some highlighted by yellow dotted lines. Figure 2h reveals the distinct lattice fringes of NCS/CS@LC_{50}, further confirming its excellent crystallinity. Moreover, the plane spacings observed at 0.255 nm for $NiCo_2S_4$ (422) and at 0.160 nm for Co_9S_8 (311), as shown in Fig. 2h, illustrated the successful integration of $NiCo_2S_4$ and Co_9S_8 within the NCS/CS@LC_{50} sample.

The synthesized material was coated onto a current collector copper foil, subsequently stamped, and assembled with sodium sheets to construct a sodium-ion half-cell for evaluating its electrochemical characteristics. Initially, the assembled sodium-ion half-cell underwent CV testing within a potential window of 0.01–3 V at a scan rate of 0.01 mV s^{-1}. Figure 3a illustrates the CV curves for the initial five cycles of NCS/CS@LC_{50}, while the CV plots for the other samples are provided in Supplementary Fig. S3. The CV curve revealed distinct oxidation and reduction peaks, indicating that NCS/CS@LC_{50} exhibited favorable electrochemical activity in SIBs. In the initial CV curve, the reduction peak at 0.96 V corresponded to the insertion of Na^+ into NCS/CS@LC_{50}, while reduction peaks at 0.64 and 0.28 V were associated with the reduction and deposition of electrolyte components on the surface of the negative electrode, leading to the formation of solid-electrolyte interphase (SEI) films, as well as the reduction of Co^{2+}/Co^{3+} and Ni^{2+}/Ni^{3+} to Co and Ni, respectively[25,26]. Correspondingly, the oxidation peak at 1.82 V was associated with the oxidation of Co and Ni to form CoS_x and NiS_x. In the subsequent CV plots, the reduction and oxidation peaks detected at 1.27, 0.86, and 1.76 V, respectively, correspond to the reduction and oxidation processes of Co^{2+}/Co^{3+} and Ni^{2+}/Ni^{3+}. From the second cycle onward, the CV curves largely overlapped, indicating that NCS/CS@LC_{50} exhibited good reversibility[27]. Specifically, the insertion and extraction of Na^+ in the electrode material were reversible, with no significant changes in electrode structure or loss of active sites. Moreover, it was observed that the integral area of the CV curve during the first cycle was greater than that of subsequent cycles, indicating that the initial cycle of the electrode experienced a substantial amount of charge transfer during charging and discharging, thereby reflecting a higher specific capacity compared to later cycles. This phenomenon was further corroborated by the galvanostatic charge-discharge profile presented in Fig. 3b, c. The discharge capacity of NCS/CS@LC_{50} was 1,062.8 mAh g^{-1} during the first cycle, which gradually decreased as cycling progressed. The other samples exhibited analogous variation trends, as illustrated in Supplementary Fig. S4. The underlying reasons for this decline were as follows. The active material on the surface of NCS/CS@LC_{50} may have reacted with the electrolyte to form an SEI layer, a process that consumed some of the active material[28]. As the charge-discharge cycles continued, the ongoing formation and reconfiguration of the SEI layer may have further depleted the active material, leading to a gradual decline in specific capacity. In contrast, the initial Coulombic efficiency of NCS/CS@LC_{50} was found to be superior to that of pure NCS, which is attributed to the incorporation of lignin-derived carbon layer. This carbon layer exhibits multiple synergistic effects, such as minimizing the irreversible consumption of SEI, mitigating the adsorption at defect sites, optimizing the arrangement of sodium storage active sites, enhancing conductivity, and strengthening the stability of the electrode-electrolyte interface[29]. Consequently, these effects collectively contributed to an enhancement in the initial Coulombic efficiency of NCS/CS@LC_{50}. After 100 cycles, the specific capacities of NCS, NCS/CS@LC_{25}, NCS/CS@LC_{50}, and NCS/CS@LC_{75} were measured at 27.2, 87.5, 244.5, and 162.7 mAh g^{-1}, respectively, as illustrated in Fig. 3b. The maximum specific capacity exhibited by NCS/CS@LC_{50} indicates that its specific surface area and pore dimensions have been precisely optimized, leading to improved electrical conductivity and structural stability as well as a reduced likelihood of side reactions. The initial Coulombic efficiency (ICE) serves as a key metric for assessing electrode reversibility and energy utilization efficiency. The calculated initial efficiencies of the synthesized samples are summarized in Table 1. Furthermore, as illustrated in Fig. 3c, the Coulombic efficiency of NCS/CS@LC_{50} increased rapidly after the initial cycle for two primary reasons. This calculation result indicates that an appropriate carbon coating thickness can maximize the ICE by synergistically optimizing ion and electron transport, suppressing side reactions, and mitigating volume expansion. However, a coating that is either too thin or too thick will lead to reduced ICE. First, NCS/CS@LC_{50} may demonstrate good structural stability during charging and discharging, which helps to minimize the shedding of active materials and the decomposition of the electrolyte, thereby enhancing Coulombic efficiency[30]. Second, as the charge-discharge cycles progressed, the SEI membrane gradually stabilized, reducing electrolyte consumption and active material loss. Consequently, the Coulombic efficiency experienced a rapid increase from the second cycle onward.

Figure 3d illustrates the rate performance of NCS/CS@LC_{50}, which outperformed all other samples. At current densities of 0.1, 0.2, 0.5, 1, and 2 A g^{-1}, the average discharge specific capacities were measured at 548.2, 423.3, 328.1, 247.1, and 208.7 mAh g^{-1}, respectively. Upon decreasing the current density to 0.1 A g^{-1}, the specific capacity was restored to 332.2 mAh g^{-1}, rather than the initial 548.2 mAh g^{-1}. The irreversible capacity loss may be attributed to lattice stress in electrode materials under high-rate operation, intensified interfacial side reactions, increased polarization, and the shedding or dissolution of active materials. Under high current charge and discharge conditions, the transport of Na^+ and electrons within the anode material may have been constrained, leading to some active substances being unable to participate in electrochemical reactions promptly[31]. Additionally, the anode material may have undergone significant volume changes or structural stresses. Moreover, it is essential for the anode material to possess rapid kinetic response capabilities to facilitate swift electrochemical reactions[32]. Consequently, as the current increased, the specific capacity tended to decrease. When the current was reduced, a rapid kinetic response from the anode material allowed for the recovery of specific capacity. This observation indicated that NCS/CS@LC_{50} had effective ion and electron transport pathways capable of supporting rapid electrochemical reactions. NCS/CS@LC_{50} could also maintain good structural stability after undergoing high-current charging and discharging cycles without severe structural damage or performance degradation. Furthermore, NCS/CS@LC_{50} demonstrated commendable kinetic properties and stable electrochemical activity

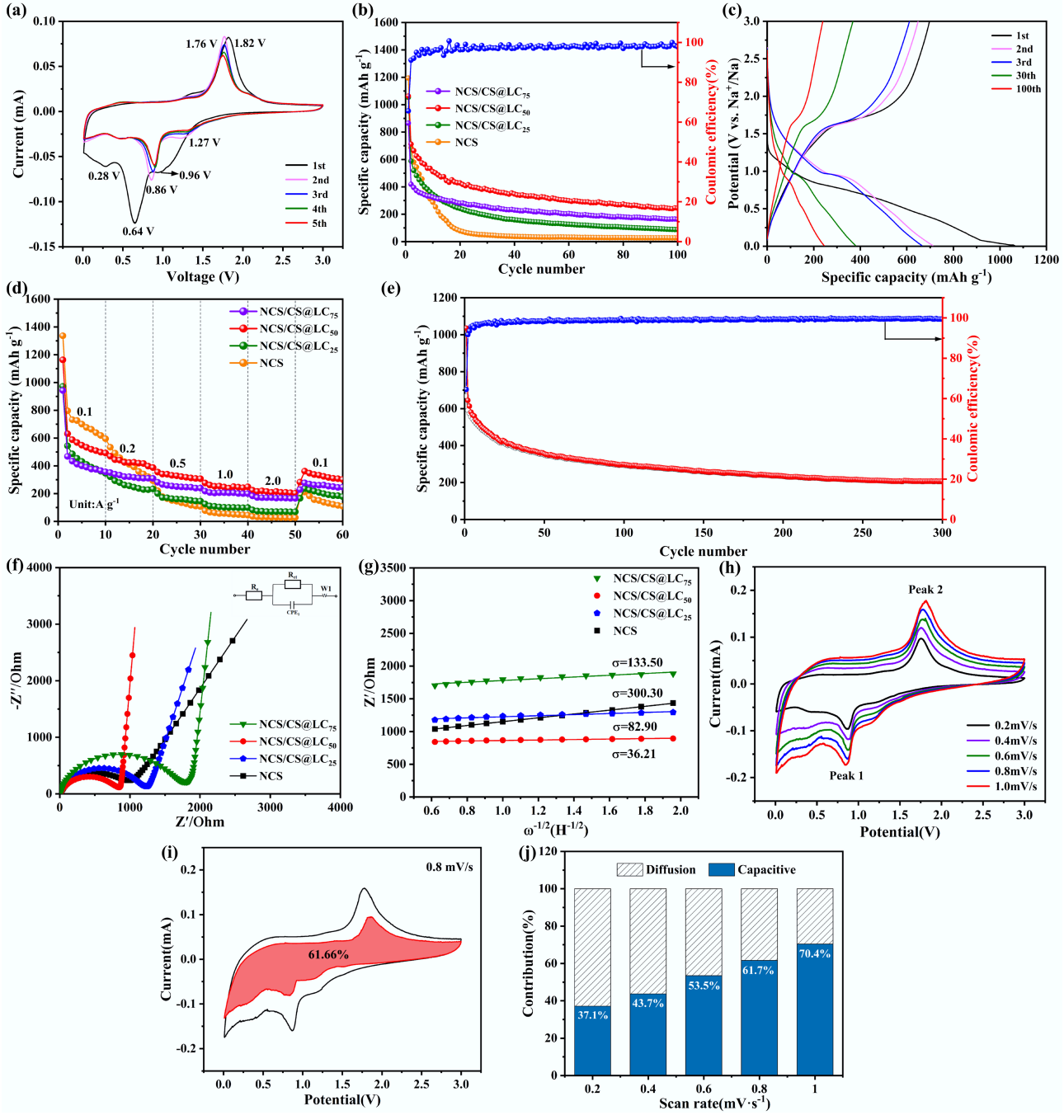

Fig. 3 (**a**) CV plot of first five cycles for NCS/CS@LC_{50}. (**b**) Constant current charge-discharge profile of NCS/CS@LC_{50} at a current of 0.1 A g^{-1}. (**c**) Capacity-voltage curve of NCS/CS@LC_{50} for 1st, 2nd, 3rd, 30th, and 100th. (**d**) Rate performance plot of NCS/CS@LC_{50} at various current densities (0.1, 0.2, 0.5, 1.0, 2.0, and 0.1 A g^{-1}). (**e**) Cycling performance of NCS/CS@LC_{50} at a current density of 0.5 A g^{-1}. (**f**) Nyquist diagram of synthesized NCS and NCS/CS@LC, accompanied by an equivalent circuit diagram as its illustration. (**g**) Straight line fitted between Z' and $\omega^{-1/2}$ at low frequencies for synthesized NCS and NCS/CS@LC. (**h**) CV measurements of NCS/CS@LC_{50} electrode conducted at varying scan rates. (**i**) Pseudocapacitive contribution of NCS/CS@LC_{50} electrode evaluated at a scan rate of 0.8 mV s^{-1}. (**j**) Ratio of pseudocapacitance control to diffusion control for NCS/CS@LC_{50} electrode at varying sweep rates.

across varying current conditions. Overall, the aforementioned phenomena and analysis indicated that NCS/CS@LC_{50} exhibited favorable ion and electron transport properties, exceptional structural stability, and promising kinetic characteristics. The long-term cycling performance of anode materials for sodium-ion batteries is a key indicator for assessing their practical applicability for Fig. 3e. It fundamentally reflects the material's ability to withstand structural degradation, accumulation of side reactions, and interfacial deterioration during repeated Na^+ intercalation and deintercalation processes. As shown in Fig. 3e, NCS/CS@LC_{50} exhibited stable cycling performance, retaining a specific capacity of 207 mAh g^{-1} after 300 cycles at a current density of 0.5 A g^{-1}, which demonstrates its excellent cycle stability. This favorable performance is attributed to the optimal thickness of the lignin-derived carbon coating, which effectively mitigates volume stress and suppresses metal ion dissolution. Furthermore, the SEM image of NCS/CS@LC_{50}

after 300 cycles revealed that its hollow mesoporous structure remained well-preserved, further confirming its excellent cycling stability (Supplementary Fig. S5).

AC impedance analysis is frequently utilized to elucidate the internal impedance characteristics of batteries and assess the reaction kinetics of the electrodes, playing a crucial role in battery research. AC impedance measurements were performed using an electrochemical workstation across a frequency range of 100 kHz to 0.01 Hz at ambient temperature, resulting in the acquisition of Nyquist plots (Fig. 3f). Each Nyquist plot exhibited a semicircle in the high-frequency range and a straight line in the low-frequency range. The semicircle in the high-frequency range primarily represented the charge transfer impedance (R_{ct}) at the electrode/electrolyte interface. During battery charging and discharging, charge must be transferred between the electrodes and the electrolyte, with the impedance of this process reflected in the high-frequency range[33]. The low-frequency range primarily reflected the diffusion process of ions within solid materials. In battery systems, ions must diffuse through solid electrode materials to participate in electrochemical reactions. The impedance associated with this process, referred to as Warburg impedance (Z_w), is typically manifested in the low-frequency range as a diagonal line[34]. Furthermore, the intercept of the Z'-axis in the high-frequency range is regarded as the electrolyte impedance (R_e)[35]. The EIS spectra were meticulously analyzed using an equivalent circuit model with the aid of Zview software. The R_{ct} values of NCS, NCS/CS@LC_{25}, NCS/CS@LC_{50}, and NCS/CS@LC_{75} were 855.3, 1,144.0, 790.3, and 1,651.0 Ω, respectively. The results indicated that the R_{ct} of NCS/CS@LC_{50} was the lowest, attributable to three key factors. First, the regular and uniform honeycomb-like structure of NCS/CS@LC_{50} facilitated a shorter diffusion path for ions, thereby reducing the R_{ct}. Second, the synergistic interaction between $NiCo_2S_4$ and Co_9S_8 may also have contributed to lowering the R_{ct} and enhancing its electrochemical performance. Third, the formation of lignin-derived carbon increased the conductivity of the material, which accelerated interfacial charge transfer and further diminished the R_{ct}[36]. This minimized energy loss during the transmission process, thereby allowing the SIBs to demonstrate superior electrochemical performance during both charging and discharging. Building upon this, the EIS data were utilized along with Eqs (1) and (2) to calculate the Na^+ diffusion coefficient (*D*)[37]. Initially, the Warburg coefficient (σ) was determined through linear fitting of Z' and $\omega^{-1/2}$, as illustrated in Fig. 3g. Subsequently, *D* was computed using Eq. (1), and the results are presented in Table 1. As anticipated, the *D* of NCS/CS@LC_{50} was found to be highest, indicating that Na^+ could be embedded into and detached from NCS/CS@LC_{50} most rapidly, thereby further validating the optimal rate performance and minimal charge transfer resistance of NCS/CS@LC_{50}.

$$D = R^2T^2/2A^2n^4F^4C^2\sigma^2 \quad (1)$$

$$Z' = R_e + R_{ct} + \sigma\omega^{-1/2} \quad (2)$$

To thoroughly assess the pseudocapacitive characteristics of NCS/CS@LC_{50} and quantify the contribution of pseudocapacitance, CV measurements were performed at various scan rates of 0.2, 0.4, 0.6, 0.8, and 1 mV s^{-1}, with results presented in Fig. 3h. It was clear that as the sweep rate increased, the peak current also rose correspondingly. According to the Randles-Sevcik equation, there exists a linear correlation between the square root of the peak current and the sweep velocity, which accounts for this observed phenomenon. Furthermore, as the scan rate increased, both the oxidation and reduction peak potentials exhibited shifts; specifically, the oxidation peak shifted towards more positive potentials while the reduction peak moved towards more negative potentials. This phenomenon was attributed to the fact that, for oxidation reactions, the concentration of electrons at the electrode surface decreases with increasing scan rate, as electrons are transferred more rapidly to the solution. To sustain the reaction, a higher electric potential is necessary to facilitate electron transfer; consequently, the oxidation peak potential shifts towards more positive values[16]. Conversely, in reduction reactions, the concentration of electrons at the electrode surface increases with rising scanning rates because electrons are transferred from the solution to the electrode more swiftly. In this scenario, a lower potential suffices to drive electron transfer, resulting in a shift of the reduction peak potential towards more negative values[38].

Additionally, the *b*-value was utilized to identify the charge storage mechanism of NCS/CS@LC_{50} throughout its charge and discharge cycles. First, the relationship between peak current (i) and sweep velocity (v), expressed as $i = av^b$, was transformed into a logarithmic form: $\log(i) = b \times \log(v) + \log(a)$. Subsequently, by performing a linear fit on log(i) and log(v), the value of b was determined and is presented in Supplementary Fig. S6; this was because b represented the slope of the fitted line. It is well-known that a *b*-value of 0.5 indicates battery-like behavior in the electrode material, with the corresponding process being governed by diffusion control. If the *b*-value is between 0.5 and 1, the electrode material displays characteristics of both battery and pseudocapacitance properties. When the *b*-value exceeds 1, it signifies that the electrode material primarily demonstrates pseudocapacitive behavior[39]. Supplementary Fig. S6 clearly shows that the *b*-value was 0.65 for the reduction peak and 0.58 for the oxidation peak. This indicated that charge storage and release occurred through both ion diffusion within NCS/CS@LC_{50} (cell behavior) and Faradaic processes at or within the electrode surface (pseudocapacitance behavior). These mechanisms contribute to enhancing the energy density, power density, and cycling stability of SIBs.

Furthermore, the pseudocapacitance contribution ratio was calculated. For each specific voltage value, k_1 and k_2 values were obtained by fitting $i/v^{1/2}$ and $v^{1/2}$ at different sweep rates using Eq. (4), which is mathematically derived from Eq. (3)[40]:

$$i = k_1v + k_2v^{1/2} \quad (3)$$

$$i/v^{1/2} = k_1v^{1/2} + k_2 \quad (4)$$

where, i stands for current, v represents scan rate, and k_1 and k_2 are the fitting parameters.

Based on the k_1 value obtained through fitting and the specific voltage value, as well as the sweep rate v, the current value contributed by the pseudocapacitor was calculated from $i_{cap} = k_1v$. Then, using the voltage as the abscissa and the i_{cap} as the ordinate, the curve of the pseudocapacitance was plotted. Next, area fitting of the pseudocapacitance curve was performed to determine its contribution rate. The fitted pseudocapacitance curve was then compared with the original CV curve, allowing us to analyze the contribution of pseudocapacitive behavior to the total current[41]. The results are presented in Fig. 3i, j. As illustrated in Fig. 3i, pseudocapacitive behavior accounted for 61.66% of the total current at a sweep speed of 0.8 mV s^{-1}. Additionally, it was evident from Fig. 3j that the contribution rate of pseudocapacitance increased with higher sweep rates. A high contribution rate enabled charge to be rapidly stored and released on or near the surface area of NCS/CS@LC_{50}, enhancing both charge-discharge rates and energy output for the battery while improving cycle stability[42]; this allowed Na^+ to embed and detach more rapidly, thereby boosting the battery's rate performance.

To elucidate the impact of the newly formed Co_9S_8 phase on the electrochemical performance of $NiCo_2S_4$ at the microstructural level, systematic calculations and analyses of electronic interactions at the $NiCo_2S_4/Co_9S_8$ interface were conducted using density functional theory (DFT). As illustrated in Fig. 4a and b, the Fermi level of $NiCo_2S_4$ was calculated to be −1.156 eV, which was marginally higher than that of Co_9S_8 (−1.719 eV). This subtle difference in energy levels exerts a notable influence when the two materials form a heterojunction[43]. Once the generated Co_9S_8 is coated onto $NiCo_2S_4$, a contact potential difference forms at the interface, facilitating electron transfer from the inner $NiCo_2S_4$ to the outer Co_9S_8. From the standpoint of electronic work function analysis, the $NiCo_2S_4/Co_9S_8$ heterostructure exhibited a work function of 5.305 eV (as depicted in Fig. 4c), which was intermediate between those of pure $NiCo_2S_4$ (5.111 eV) and pure Co_9S_8 (5.951 eV). This observation suggests that the electromotive force of $NiCo_2S_4/Co_9S_8$ is predominantly governed by Co_9S_8, highlighting the critical influence of Co_9S_8 in determining the overall electrochemical performance of $NiCo_2S_4/Co_9S_8$[43]. Figure 4d presents the charge density difference for the interface of $NiCo_2S_4/Co_9S_8$, showing that sulfur atoms located in the shell layer donate electrons, whereas cobalt atoms supply holes, thereby establishing a charge transfer pathway. Furthermore, these shell-layer sulfur atoms engage in additional charge transfer pathways with both nickel and cobalt atoms situated in the core layer. The density of states (DOS) and band structure of $NiCo_2S_4/Co_9S_8$ were computed to obtain a more comprehensive understanding of its intrinsic electronic properties. The band structure presented in Fig. 4f aligns well with the corresponding DOS profile (Fig. 4e), as regions exhibiting pronounced DOS peaks correspond to densely populated segments of the band structure[44]. The electronic states near the Fermi level predominantly arise from Ni-3d, Co-2p, and S-2p orbitals. The elevated DOS near the Fermi level of $NiCo_2S_4/Co_9S_8$ suggests that this composite exhibits superior electrical conductivity[45]. Combined with the favorable conductive properties of lignin-derived carbon, this feature contributes to the enhanced sodium storage performance of $NiCo_2S_4/Co_9S_8$@LC. The bandgap configuration (0.527 eV), as shown in Fig. 4e, is sufficiently wide to prevent the reduction of open-circuit voltage that typically arises from an excessively narrow bandgap. The relatively wide bandgap contributes to mitigating energy losses associated with non-radiative recombination during electrochemical processes, thereby enhancing the overall energy conversion efficiency[43]. Thus, DFT-based theoretical calculations reveal that $NiCo_2S_4/Co_9S_8$@LC possesses superior electronic transport properties and low charge transfer resistance, endowing it with significant potential as an anode material for SIBs.

Ultimately, the sodium storage performance of $NCS/CS@LC_{50}$ synthesized from spent mobile phone batteries and modified with lignin-derived carbon was evaluated against previously reported data (Table 2). The results demonstrated that its electrochemical performance is comparable or slightly inferior to that of previously reported $NiCo_2S_4$ prepared by analytic reagents. However, this study successfully achieved the high-value utilization of waste resources. The resulting material, $NCS/CS@LC_{50}$, exhibits excellent sodium storage performance while being derived from sustainable and environmentally benign feedstocks, demonstrating its significant potential for industrial application. This approach not only substantially reduces the manufacturing cost and enhances the market competitiveness of SIBs but also facilitates their large-scale deployment in smart grids, electric vehicles, and various electronic devices.

Conclusions

In this research, $NCS/CS@LC_{50}$ was prepared via a hydrothermal process utilizing spent mobile phone batteries and industrial lignin as the primary raw materials. The composite integrated the high

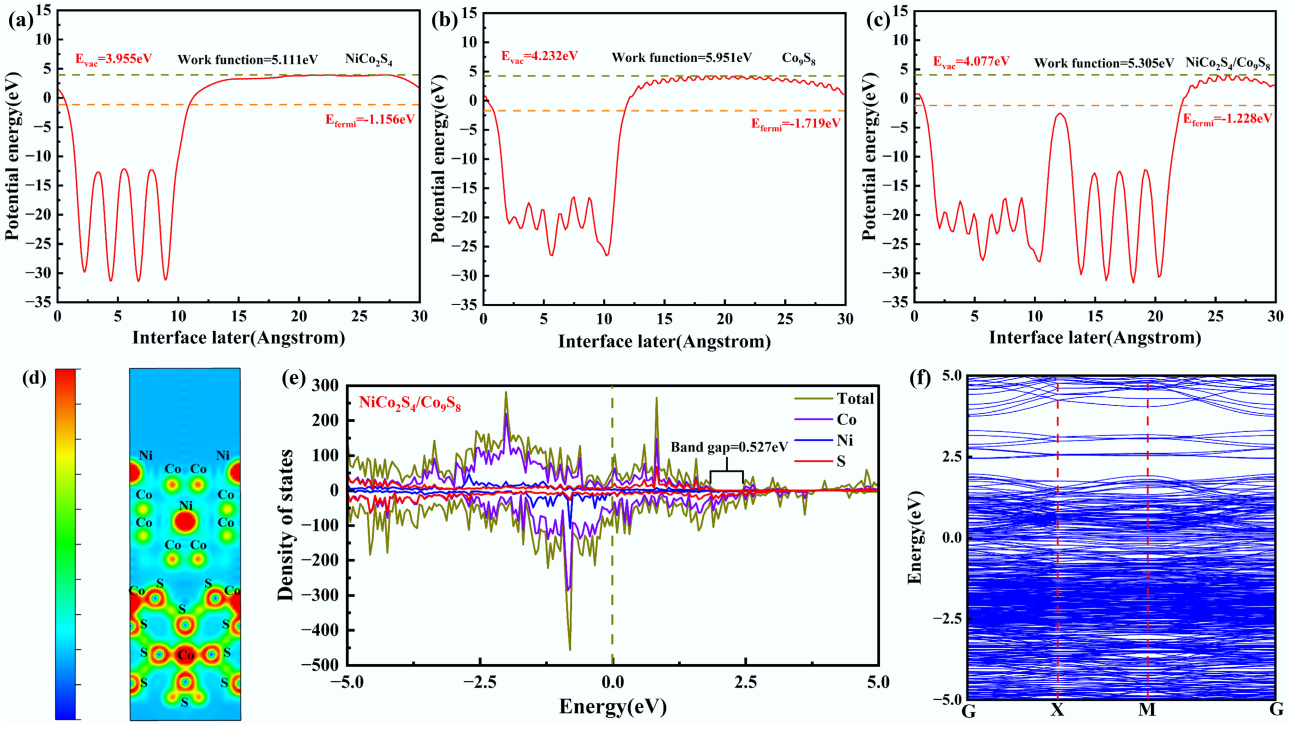

Fig. 4 Calculated work function of (**a**) $NiCo_2S_4$, (**b**) Co_9S_8, and (**c**) $NiCo_2S_4/Co_9S_8$. (**d**) Charge density difference for the interface of $NiCo_2S_4/Co_9S_8$. (**e**) Density of state, and (**f**) band structure for $NiCo_2S_4/Co_9S_8$.

Table 2 Comparison of the electrochemical performance of the synthesized NCS/CS@LC_{50} in this study with that of $NiCo_2S_4$ reported in the literature

Materials	Current density ($A\ g^{-1}$)	Specific capacity ($mAh\ g^{-1}$)/ cycle number	Ref.
$NiCo_2S_4$@CNTs	0.05	291/80	[46]
$NiCo_2S_4$@CNF	2.0	283/400	[47]
$NiCo_2S_4$@Ni-B	1.0	252/200	[48]
$NiCo_2S_4$@MoS_2	3.2	158/400	[49]
NCS@GNs@CNTs	0.2	363/100	[50]
NCSGO	1.0	250/350	[51]
$NiCo_2S_4$/Co_9S_8@LC_{50}	1.0	245/100	This work

electrochemical activity of $NiCo_2S_4$ and Co_9S_8 with the excellent electrical conductivity of carbon materials, presenting unique structural and performance advantages. Electrochemical testing revealed that the NCS/CS@LC_{50} demonstrated high reversible specific capacity, good cycling stability, and exceptional rate performance. These enhancements in performance were primarily attributed to the synergistic effects of its various components and the distinctive structure of this composite. Specifically, $NiCo_2S_4$ and Co_9S_8 provided a rich array of redox reaction sites, facilitating the Na^+ intercalation/deintercalation; additionally, the incorporation of carbon materials enhanced overall electrode conductivity, promoting rapid electron transport. Furthermore, this study considered the effect of lignin-derived carbon on the morphology of NCS/CS@LC, providing valuable references for further optimizing the performance of composite materials. Simultaneously, the feasibility of utilizing spent mobile phone batteries and industrial lignin as raw materials to prepare high-performance sodium storage materials was also validated, providing a new perspective on the resource utilization of spent batteries and industrial lignin.

Supplementary information

It accompanies this paper at: https://doi.org/10.48130/bchax-0026-0005.

Author contributions

The authors confirm their contributions to the paper as follows: Changwei Dun: conceptualization, investigation, methodology, formal analysis, writing – original draft, funding acquisition, resources, writing – review and editing; Yizhao Zhao: investigation, methodology, data curation; Pengpeng Zhang: conceptualization, investigation, formal analysis, data curation; Hua Lv: conceptualization, resources; Yumin Li: methodology, supervision; Yuebin Xi: funding acquisition, supervision, methodology, formal analysis, writing – review and editing; Xijun Zhang: resources, conceptualization, investigation; Rui Liang: conceptualization, supervision. All authors reviewed the results and approved the final version of the manuscript.

Data availability

All data generated or analyzed during this study are included in this published article and its supplementary information files.

Funding

This research was supported by the Postdoctoral Research Funds from Henan Province (Grant No. 5101039470652); collaborative scientific research projects with Henan Nuofei Biotechnology Co., Ltd (Grant Nos 5201039160188 and 5201039160224); National Natural Science Foundation of China (Grant No. 22108135); Natural Science Foundation of Shandong Province (Grant Nos ZR2024MB12 and ZR2020QB197); Shandong University youth innovation team (Grant No. 2023KJ137).

Declarations

Competing interests

The authors declare that they have no known competing financial interests or personal relationships that could have appeared to influence the work reported in this paper.

Author details

[1]Henan Key Laboratory of Green Chemistry, Collaborative Innovation Center of Henan Province for Green Manufacturing of Fine Chemicals, Key Laboratory of Green Chemical Media and Reactions, Ministry of Education, School of Chemistry and Chemical Engineering, Henan Normal University, Xinxiang 453007, China; [2]Department of Light Industry, State Key Laboratory of Green Papermaking and Resource Recycling, Qilu University of Technology (Shandong Academy of Sciences), Jinan 250353, China

References

[1] Sarkar M, Hossain R, Sahajwalla V. 2024. Sustainable recovery and resynthesis of electroactive materials from spent Li-ion batteries to ensure material sustainability. *Resources, Conservation and Recycling* 200:107292

[2] Liu Y, Jiao B, Guo X, Li S, Lou X, et al. 2024. Retrieving lost Li in LIBs for co-regeneration of spent anode and cathode materials. *Energy Storage Materials* 72:103684

[3] Espinoza-Acosta JL, Torres-Chávez PI, Olmedo-Martínez JL, Vega-Rios A, Flores-Gallardo S, et al. 2018. Lignin in storage and renewable energy applications: a review. *Journal of Energy Chemistry* 27:1422–1438

[4] Tang Q, Qian Y, Yang D, Qiu X, Qin Y, et al. 2020. Lignin-based nanoparticles: a review on their preparations and applications. *Polymers* 12:2471

[5] Cao D, Zhang Q, Hafez AM, Jiao Y, Ma Y, et al. 2019. Lignin-derived holey, layered, and thermally conductive 3D scaffold for lithium dendrite suppression. *Small Methods* 3:1800539

[6] Zhang P, Zhang G, Liu Y, Fan Y, Shi X, et al. 2024. Constructing P_2/O_3 biphasic structure of Fe/Mn-based layered oxide cathode for high-performance sodium-ion batteries. *Journal of Colloid and Interface Science* 654:1405–1416

[7] Zeng Z, Mao Y, Hu Z, Chen K, Huang Q, et al. 2023. Research progress and commercialization of biologically derived hard carbon anode materials for sodium-ion batteries. *Industrial & Engineering Chemistry Research* 62:15343–15359

[8] Sun Z, Zhao C, Cao X, Zeng K, Ma Z, et al. 2020. Insights into the phase transformation of NiCo2S4@rGO for sodium-ion battery electrode. *Electrochimica Acta* 338:135900

[9] Xi JC, Yuan YF, Yang JL, Chen YB, Shen SH, et al. 2024. $NiCo_2S_4$ nanoparticles encapsulated within hollow mesoporous carbon spheres enabling rapid and stable sodium storage. *Journal of Energy Storage* 102:114216

[10] Jiang Z, Xu Z, Li L, Wei J, Liu Q, et al. 2025. Design principles for efficient hydrothermal relithiation of spent lithium iron phosphate. *ACS Applied Materials & Interfaces* 17:4875–4883

[11] Dun C, Zhang P, Liu Y, Lv H, Liang R, et al. 2024. Effect of polypyrrole-derived N-doped carbon coating on the sodium storage properties of $NiCo_2S_4$ synthesized by recycling discarded mobile phone batteries. *Ceramics International* 50:32717–32726

[12] Wang S, Pang X, Huang D, Zhang M, Hu S, et al. 2025. Construction of Co_9S_8@C-MoS_2 heterostructure for fast charging and superior long-term cycling performance of sodium ion batteries. *Journal of Colloid and Interface Science* 680:398–406

[13] Liao C, Hou Y, Han L, Zhu Y, Wang H, et al. 2022. Expandable nitrogen-doped carbon-based anodes fabricated from self-sacrificial metal-organic frameworks for ultralong-life lithium storage. *Carbon* 186:46–54
[14] Wang H, Hu L, Wang C, Sun Q, Li H, et al. 2019. High-loading individually dispersed $NiCo_2O_4$ anchoring on checkerboard-like C/CNT nanosheets as a binder-free high rate electrode for lithium storage. *Journal of Materials Chemistry A* 7:3632–3641
[15] Zhu YL, Wang YX, Gao C, Zhao WN, Wang XB, et al. 2020. $CoMoO_4$-N-doped carbon hybrid nanoparticles loaded on a petroleum asphalt-based porous carbon for lithium storage. *New Carbon Materials* 35:358–370
[16] Jeon Y, Lee J, Jo H, Hong H, Lee LYS, et al. 2021. Co/Co_3O_4-embedded N-doped hollow carbon composite derived from a bimetallic MOF/ZnO Core-shell template as a sulfur host for Li-S batteries. *Chemical Engineering Journal* 407:126967
[17] Zhang W, Lan C, Xie X, Cao Q, Zheng M, et al. 2019. Facile construction of hollow carbon nanosphere-interconnected network for advanced sodium-ion battery anode. *Journal of Colloid and Interface Science* 546:53–59
[18] Niitani K, Ushiroda S, Kuwata H, Hozumi M, Matsunaga T, et al. 2024. Communication—high-capacity hard carbons enabled by a sodium carborane solid electrolyte for sodium-ion batteries. *Journal of The Electrochemical Society* 171:010511
[19] Ud Din MA, Irfan S, Jamil S, Dar SU, Khan QU, et al. 2022. Graphene-like ultrathin bismuth selenide nanosheets as highly stable anode material for sodium-ion battery. *Journal of Alloys and Compounds* 901:163572
[20] Yan J, Li Q, Hao Y, Dai C, Chen Y. 2020. MoS_2/SnS_2 nanocomposite as stable sodium-ion battery anode. *Functional Materials Letters* 13:1950095
[21] Wu W, Zhao C, Wang C, Liu T, Wang L, et al. 2021. Hierarchical structure of Self-Supported NiCo2S4 Nanoflowers@NiCo2S4 nanosheets as high rate-capability and cycling-stability electrodes for advanced supercapacitor. *Applied Surface Science* 563:150324
[22] Cai K, Li Y, Lang X, Li L, Zhang Q. 2019. Synergistic effect of sulfur on electrochemical performances of carbon-coated vanadium pentoxide cathode materials with polyvinyl alcohol as carbon source for lithium-ion batteries. *International Journal of Energy Research* 43:7664–7671
[23] Cai F, Sun C, Sun Z, Lai Y, Ding H. 2023. Sulfur-functionalized $CoMn_2O_4$ as a Fenton-like catalyst for the efficient rhodamine B degradation. *Applied Surface Science* 623:157044
[24] Zhang C, Xie Z, Yang W, Liang Y, Meng D, et al. 2020. $NiCo_2O_4$/biomass-derived carbon composites as anode for high-performance lithium ion batteries. *Journal of Power Sources* 451:227761
[25] Lu X, Liu A, Zhang Y, Liu S. 2020. Space-confined synthesis of yolk–shell structured Co_3O_4/nitrogen-doped carbon nanocomposites with hollow mesoporous carbon nanocages as advanced functional anodes for lithium-ion batteries. *ACS Applied Energy Materials* 3:11153–11163
[26] Jiao X, Cai L, Xia X, Lei W, Hao Q, et al. 2019. Novel spinel nanocomposites of $Ni_xCo_{1-x}Fe_2O_4$ nanoparticles with N-doped graphene for lithium ion batteries. *Applied Surface Science* 481:200–208
[27] Gong Y, Sun L, Si H, Zhang Y, Shi Y, et al. 2020. MnO nanorods coated by co-decorated N-doped carbon as anodes for high performance lithium ion batteries. *Applied Surface Science* 504:144479
[28] Sun J, Gunathilaka IE, O'dell LA, Howlett PC, Forsyth M. 2023. High-rate formation protocol enables a high ionic conductivity SEI for sodium-ion batteries. *Journal of Power Sources* 554:232298
[29] Liu Y, Que X, Wu X, Yuan Q, Wang H, et al. 2020. ZIF-67 derived carbon wrapped discontinuous Co_xP nanotube as anode material in high-performance Li-ion battery. *Materials Today Chemistry* 17:100284
[30] Lu X, Liu A, Zhang Y, Liu S. 2021. A yolk-shell structured CoS_2@NC@CNC with double carbon shell coating from confined derivatization of ZIF-67 growth in carbon nanocages for superior Li storage. *Electrochimica Acta* 371:137773
[31] Zhang P, Feng Y, Cao M, Yao J. 2020. Construction of sandwich-type Co_9S_8-C anchored on carbonized melamine foam toward lithium-ion battery. *Electrochimica Acta* 363:137220
[32] Gou H, Li W, Yang Y, Li X, Cui H, et al. 2021. Porous skeleton-stabilized Co/N–C coated separator for boosting lithium-ion batteries stability and safety. *Journal of Power Sources* 499:229933
[33] Hu L, Zheng S, Cheng S, Chen Z, Huang B, et al. 2019. $CrPO_4$/C composite as a novel anode material for lithium-ion batteries. *Journal of Power Sources* 441:227180
[34] Li Y, Meng Y, Liu X, Xiao M, Hu Q, et al. 2019. Double-protected zinc ferrite nanospheres as high rate and stable anode materials for lithium ion batteries. *Journal of Power Sources* 442:227256
[35] Miao Y, Zhao X, Wang X, Ma C, Cheng L, et al. 2020. Flower-like $NiCo_2S_4$ nanosheets with high electrochemical performance for sodium-ion batteries. *Nano Research* 13:3041–3047
[36] Mubasher, Mumtaz M, Hassan M, Ullah S, Ahmad Z. 2021. Nanohybrids of multi-walled carbon nanotubes and cobalt ferrite nanoparticles: high performance anode material for lithium-ion batteries. *Carbon* 171:179–187
[37] Li H, Luo J, Han D, Liu A, Zhou M, et al. 2023. Layer-by-layer heterocarbon modifying ZnS nanocubes anode with improved long-term life for sodium-ion batteries. *Ceramics International* 49:18421–18431
[38] Zhang LL, Ma D, Li T, Liu J, Ding XK, et al. 2018. Polydopamine-derived nitrogen-doped carbon-covered $Na_3V_2(PO_4)_2F_3$ cathode material for high-performance Na-ion batteries. *ACS Applied Materials & Interfaces* 10:36851–36859
[39] Lim YV, Huang S, Wu Q, Kong D, Wang Y, et al. 2020. Super kinetically pseudocapacitive $MnCo_2S_4$ nanourchins toward high-rate and highly stable sodium-ion storage. *Advanced Functional Materials* 30:1909702
[40] Chen H, Tian P, Fu L, Wan S, Liu Q. 2022. Hollow spheres of solid solution $Fe_7Ni_3S_{11}$/CN as advanced anode materials for sodium ion batteries. *Chemical Engineering Journal* 430:132688
[41] Yan W, Liang K, Chi Z, Liu T, Cao M, et al. 2021. Litchi-like structured $MnCo_2S_4$@C as a high capacity and long-cycling time anode for lithium-ion batteries. *Electrochimica Acta* 376:138035
[42] Wang J, Yue X, Liu Z, Xie Z, Zhao Q, et al. 2022. Trimetallic sulfides derived from tri-metal-organic frameworks as anode materials for advanced sodium ion batteries. *Journal of Colloid and Interface Science* 625:248–256
[43] Gong J, Luo W, Zhao Y, Xie M, Wang J, et al. 2022. Co_9S_8/$NiCo_2S_4$ core-shell array structure cathode hybridized with PPy/MnO_2 core-shell structure anode for high-performance flexible quasi-solid-state alkaline aqueous batteries. *Chemical Engineering Journal* 434:134640
[44] Lv H, Zhou C, Shen Q, Kong Y, Wan B, et al. 2025. Rationally designed $CaTiO_3$/$Mn_{0.5}Cd_{0.5}S$/Ni_3C S-scheme/Schottky integrated heterojunction for efficient photocatalytic H_2 evolution. *Journal of Colloid and Interface Science* 677:365–376
[45] Lv H, Zhang F, Wang L, Shen Q, Li G, et al. 2024. Construction of 2D/1D Cu_7S_4 nanosheets/$Mn_{0.3}Cd_{0.7}S$ nanorods heterojunction for highly efficient photocatalytic hydrogen evolution. *Journal of Colloid and Interface Science* 653:1304–1316
[46] Fan S, Liu H, Bi S, Gao C, Meng X, et al. 2021. Insight on the conversion reaction mechanism of $NiCo_2S_4$@CNTs as anode materials for lithium ion batteries and sodium ion batteries. *Electrochimica Acta* 388:138618
[47] Yang X, Cai T, Yao Z, Chao G. 2025. Novel $NiCo_2S_4$ nanorod arrays grown on carbon nanofibers as high-performance anodes for sodium-ion batteries. *Ionics* 31:1555–1560
[48] Li J, Zhou J, Zhou Q, Wang X, Guo C, et al. 2021. Promoting the Na^+-storage of $NiCo_2S_4$ hollow nanospheres by surfacing Ni–B nanoflakes. *Journal of Materials Science & Technology* 82:114–121
[49] Liu B, Kong D, Wang Y, Lim YV, Huang S, et al. 2018. Three-dimensional hierarchical $NiCo_2S_4$@MoS_2 heterostructure arrays for high performance sodium ion battery. *FlatChem* 10:14–21
[50] Fan S, Liu H, Bi S, Meng X, Wang Q, et al. 2023. $NiCo_2S_4$ nanoparticles anchored in the 3D interpenetrating framework composed of GNs and CNTs toward enhanced sodium storage performance. *Electrochimica Acta* 441:141760
[51] Lim YV, Huang S, Hu J, Kong D, Wang Y, et al. 2019. Explicating the sodium storage kinetics and redox mechanism of highly pseudocapacitive binary transition metal sulfide via operando techniques and Ab initio evaluation. *Small Methods* 3:1900112